# Space and momentum correlations between electrons and positrons created in Schwinger processes

C. Gong,[1] X. Y. Lu,[1] L.-N. Hu,[2] and Q. Z. Lv[2,*]

[1]Department of Mathematics and Physics, North China Electric Power University, Baoding 071003, People's Republic of China

[2]Graduate School, China Academy of Engineering Physics, Beijing 100193, People's Republic of China

(Received 27 January 2026; accepted 12 May 2026; published 10 July 2026)

We investigate the quantum correlation effects between electrons and positrons produced via Schwinger tunneling in localized supercritical electric fields. Using the framework of computational quantum field theory, we calculate the two-particle correlation functions in both momentum and real space. Our results demonstrate that the generated electron-positron pairs exhibit strong mutual correlations that evolve dynamically. In momentum space, the correlation function increases in magnitude over time while maintaining its characteristic profile. In real space, the correlation function undergoes spatial spreading without a reduction in peak amplitude. This persistence indicates that the correlation strength remains robust even as the pairs propagate beyond the localized interaction region. These findings suggest that quantum correlations in the Schwinger process are experimentally accessible, offering new opportunities to probe many-body effects under extreme field conditions.

DOI: 10.1103/4g7d-6bj6

## I. INTRODUCTION

In classical physics, correlations represent the statistical or dynamical relationships between measurable quantities arising from shared causal origins or deterministic interactions [1]. Governed by continuous laws of motion and local causality, classical correlations serve as fundamental descriptors in statistical mechanics for fluctuations and transport phenomena [2,3]. In electrodynamics and optics, they characterize coherence, quantifying how field amplitudes and phases maintain order across space and time to produce interference and diffraction [4,5]. Similarly, in fluid dynamics, velocity correlation tensors are essential for quantifying the evolution and interaction of turbulent structures [6,7]. Overall, classical correlation analysis bridges microscopic dynamics with macroscopic observables, providing a window into how local interactions generate collective behavior.

Quantum correlations, by contrast, describe connections between measurement outcomes that often defy classical intuition [8]. Beyond simple statistical dependence, these correlations manifest as quantum entanglement, where the state of a particle remains inseparably linked to its partner regardless of spatial separation [9]. Arising from the superposition principle and the structure of the quantum wave function, these correlations lead to joint probability distributions that violate Bell's inequalities, precluding any explanation based on local hidden variable theories [10]. Beyond entanglement, quantum correlations are central to phenomena such as quantum coherence [11], squeezing [12], and quantum discord [13], each representing unique modalities of information sharing within quantum systems.

A particularly frontier regime for quantum correlations is found where electromagnetic fields approach or exceed the Schwinger limit $E_s = c^3$ [14]. Henceforth, we adopt atomic units (a.u.) with $\hbar = m = -e = 1$, unless stated otherwise. In these extreme conditions, such as ultra-intense laser pulses or near astrophysical objects like magnetars, interactions become highly nonlinear and electron-positron pairs are generated directly from the vacuum via the nonperturbative Schwinger mechanism. Because these particles originate from the same quantum event, they are intrinsically correlated [15–20]. While such correlations offer a rigorous test of fundamental quantum electrodynamics (QED) predictions, the existing studies have focused almost exclusively on spin and polarization degrees of freedom [21–23].

Despite the progress in correlated spin and polarization degrees of freedom, the correlations of electron-positron pairs in real space and momentum space remain largely unexplored. They are critical, as they directly reflect the localization characteristics of the production process and the subsequent dynamical evolution of the pairs in supercritical fields. In this work, we establish a theoretical framework to describe these correlations using the computational quantum field theory (CQFT) approach [24–26]. By systematically deriving the spatial and momentum correlation functions, we provide a new perspective on

*Contact author: qzlv@gscaep.ac.cn

 

the physical mechanisms underlying field-induced vacuum decay.

The paper is organized as follows. In Sec. II, we detail the CQFT framework used to calculate the temporal evolution of the field operators and determine the particle distributions. In Sec. III, we derive the electron-positron correlation functions. We demonstrate that while the momentum-space correlation increases in magnitude over time, the real-space correlation undergoes spatial spreading without loss of peak amplitude—indicating a robust persistence of the correlation strength. In Sec. IV, we evaluate the reduced correlation functions and compare them with single-particle distributions, discussing the correlation effects caused by the virtual pairs in the vacuum. We close with a conclusion and a discussion of future problems in Sec. V.

## II. COMPUTATIONAL QUANTUM FIELD THEORY FRAMEWORK

The dynamics of the electron-positron field operator $\hat{\Psi}(\mathbf{r},t)$ are governed by the time-dependent Dirac equation [27,28], $i\frac{\partial\hat{\Psi}(\mathbf{r},t)}{\partial t} = \hat{H}\,\hat{\Psi}(\mathbf{r},t)$, where the Hamiltonian $\hat{H}$ in the presence of an external electromagnetic field is given by

$$H = c\boldsymbol{\alpha}\cdot\left[\hat{\boldsymbol{p}} - \frac{e}{c}\mathbf{A}(\mathbf{r},t)\right] + \beta m_e c^2 + eV(\mathbf{r},t). \quad (1)$$

Here, $\boldsymbol{\alpha} = (\alpha_1,\alpha_2,\alpha_3)$ and $\beta$ denote the set of standard $4\times 4$ Dirac matrices. To study the Schwinger process, we consider a localized supercritical electric field where the potential $V(\mathbf{r})$ varies only along the $x$ axis and $\mathbf{A}(\mathbf{r},t) = 0$. Consequently, the transverse canonical momenta $p_y$ and $p_z$ are conserved and there is no dynamics in the $y$- and $z$ directions. Therefore, we restrict our analysis to the $p_y = p_z = 0$ sector. In this $(1+1)$-dimensional system, the $z$ component of the spin commutes with the Dirac Hamiltonian and is therefore conserved. The two spins thus decouple from each other and do not influence the spatial and momentum correlations of interest. In this case, the Dirac field can be effectively described by a two-component spinor. The reduced Hamiltonian simplifies to

$$H = c\sigma_1 p_x + \sigma_3 c^2 - \sigma_0 V(x), \quad (2)$$

where $\sigma_i$ denote the set of the $2\times 2$ Pauli matrices that satisfy the anticommutation relations $\{\sigma_i,\sigma_j\} = 2\delta_{ij}$, and $\sigma_0$ is the identity matrix.

In the CQFT framework, we expand the time-evolved field operator $\hat{\Psi}(x,t)$ in terms of the field-free energy eigenfunctions $\{\varphi_p,\varphi_n\}$ of the Dirac Hamiltonian,

$$\hat{\Psi}(x,t) = \sum_p \hat{b}_p(t)\varphi_p(x) + \sum_n \hat{d}_n^\dagger(t)\varphi_n(x), \quad (3)$$

where $p$ and $n$ denote the positive and negative energy states of the continuum, respectively. The operators $\hat{b}_p(t)$ and $\hat{d}_n^\dagger(t)$ represent the time-dependent electron annihilation and positron creation operators. Following the Heisenberg picture, the time-dependent operators can be expressed as a linear transformation of the initial operators $(t = 0)$,

$$\hat{b}_p(t) = \sum_{p'} \hat{b}_{p'} G(p,p') + \sum_{n'} \hat{d}_{n'}^\dagger G(p,n'), \quad (4)$$

$$\hat{d}_n^\dagger(t) = \sum_{p'} \hat{b}_{p'} G(n,p') + \sum_{n'} \hat{d}_{n'}^\dagger G(n,n'), \quad (5)$$

where $\hat{b}_{p'}$ and $\hat{d}_{n'}^\dagger$ fulfill the anticommutation relationship for fermions. The dynamics are entirely encapsulated in the transition matrix elements $G(\xi,\zeta) = \langle\varphi_\xi(x)|\phi_\zeta(x,t)\rangle$, where $\phi_\zeta(x,t)$ is the solution to the time-dependent Dirac equation with the initial condition $\phi_\zeta(x,0) = \varphi_\zeta(x)$. These coefficients satisfy the unitarity relation $\sum_{k\in\{p,n\}} G(\xi,k)G^*(\zeta,k) = \delta_{\xi,\zeta}$, ensuring the preservation of the fermionic anticommutation relations: $\{\hat{b}_p(t), \hat{b}_{p'}^\dagger(t)\} = \delta_{p,p'}$ and $\{\hat{d}_n(t), \hat{d}_{n'}^\dagger(t)\} = \delta_{n,n'}$.

Adopting the Dirac hole theory, the initial vacuum state $|\mathrm{vac}\rangle$ is defined by a completely filled negative-energy sea. The momentum distribution of the created electrons at time $t$ is obtained by taking the expectation value,

$$\rho(p,t) = \langle\mathrm{vac}|\hat{b}_p^\dagger(t)\hat{b}_p(t)|\mathrm{vac}\rangle = \sum_n |G(p,n)|^2. \quad (6)$$

The total number of created pairs is then

$$N(t) = \sum_p \rho(p,t) = \sum_{p,n} |G(p,n)|^2. \quad (7)$$

The electronic component of the field operator is defined as $\hat{\Psi}_e(x,t) = \sum_p \hat{b}_p(t)\varphi_p(x)$, where $\varphi_p(x)$ are the field-free positive-energy eigenfunctions of the Dirac Hamiltonian. Then the spatial distribution of the created electron density is given by the expectation value of the density operator,

$$\begin{aligned}\rho(x,t) &= \langle\mathrm{vac}|\hat{\Psi}_e^\dagger(x,t)\hat{\Psi}_e(x,t)|\mathrm{vac}\rangle\\ &= \sum_n \left|\sum_p G(p,n)\varphi_p(x)\right|^2. \quad (8)\end{aligned}$$

While defining particle species within a strong interaction zone is non-trivial due to vacuum polarization, our localized field allows for a clear asymptotic definition of particles as they propagate into the field-free regions.

The transition matrix $G(\xi, \zeta)$ is obtained by numerically evolving the field free energy basis states under Hamiltonian Eq. (2) on a space-time lattice. We utilize a split-operator method [29,30], which provides high accuracy and efficiency for solving the $(1+1)$-dimensional Dirac equation. In the simulations, the localized supercritical electric field is modeled by a Sauter-type potential [31] $V(x) = V_0/2[1 + \tanh(x/W)]$. This potential is chosen because its corresponding electric field $E(x) = -\frac{dV}{dx} = -\frac{V_0}{2W}\mathrm{sech}^2(\frac{x}{W})$ is spatially localized and vanishes as $|x| \to \infty$. The localization of the field is crucial for the present study: it allows for a well-defined asymptotic regime where free particles can be identified. By employing this potential, we capture the key dynamics of the pair production process in a finite-sized system, which is essential for the analysis of quantum correlations, which is a central goal of this work. This choice of localized field is also consistent with a standard approach in strong-field QED and Schwinger effect studies [32–36], where spatially varying external fields are commonly employed to model realistic experimental conditions.

We set the potential height $V_0 = 2.5c^2$ and the width $W$ on the order of the Compton wavelength $\lambda_c = 1/c$, ensuring the field strength $E \sim V_0/(2W)$ reaches the supercritical regime. Throughout this work, all numerical simulations are performed within a unified spatial domain with box length $L = 64\pi\lambda_c$, discretized into $N_x = 2048$ spatial grid points, yielding a spatial resolution of $dx = \lambda_c \pi/32$. Periodic boundary conditions are adopted to satisfy the fast Fourier transformation required in the split-operator spectral method. All simulations use a fixed time step $dt = \pi\tau_c/300$, ensuring identical temporal resolution across all runs. We define the Compton time as $\tau_c = \lambda_c/c$, which represents the characteristic time scale of the electron-positron pair production process.

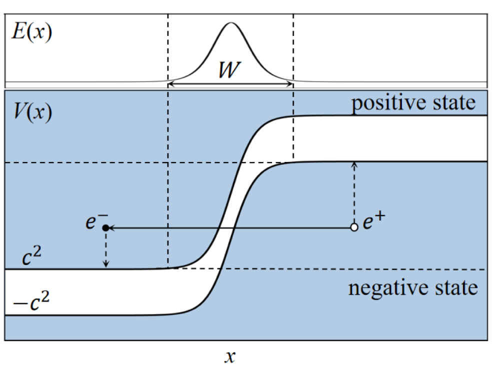


FIG. 1. Sketch of the energy spectrum for Hamiltonian Eq. (2) under the influence of the supercritical localized field $E(x)$. Because the distortion of the energy spectrum caused by the external fields, the positive and negative continuum is overlapped and triggers the pair creation.

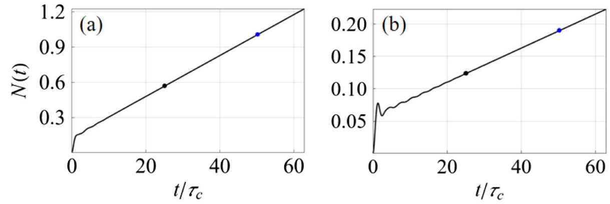


FIG. 2. Average number of particles $N(t)$ for different electric field widths as a function of time. The total evolution time is $20\pi\tau_c$. Here, $\tau_c = \lambda_c/c$ represents the typical time scale of the electron generation process. Panel (a) is for $W = 0.3\lambda_c$, while panel (b) is for $W = \lambda_c$. For this simulation, $N_x = 2048$ spatial grid points and $N_t = 6000$ temporal grid points are adopted.

The mechanism for pair production is illustrated in Fig. 1. The external potential $V(x)$ distorts the energy spectrum of the Hamiltonian, tilting the energy bands and causing an overlap between the positive and negative energy continua. This overlap creates a finite tunneling barrier, allowing fermions in the negative-energy sea to transition into positive-energy states. This process, known as Schwinger tunneling, results in the simultaneous creation of a real electron and a corresponding hole (positron) in the negative-energy sea. In the limit of a uniform field, the tunneling rate $\Gamma$ is exponentially suppressed according to the Schwinger law, $\Gamma \propto \exp(-\pi E_s/E_0)$. Consequently, significant production occurs only when the field strength $E_0$ approaches or exceeds the critical limit $E_s$.

We investigate the influence of the electric field width $W$ and the interaction time $t$ on the pair production process while maintaining a constant potential amplitude $V_0$. Figure 2 depicts the temporal evolution of the average number of created pairs, $N(t)$, for two field widths: $W = 0.3\lambda_c$ and $W = \lambda_c$. At early times, $N(t)$ exhibits a characteristic quadratic growth ($N(t) \propto t^2$), driven by the nonadiabatic "turn-on" of the external field [37]. At later times, the system enters a steady-state tunneling regime where the particle number increases linearly, defined by the constant rate $\Gamma = dN(t)/dt$.

A comparison between Figs. 2(a) and 2(b) reveals that increasing the field width $W$ while keeping $V_0$ constant leads to a decrease in the effective field strength $E_0 \sim V_0/2W$, thereby reducing the production rate. Our numerical results yield $\Gamma_{(a)} \approx 328$ and $\Gamma_{(b)} \approx 49$ for $W = 0.3\lambda_c$ and $W = \lambda_c$, respectively.

To analyze the space and momentum distribution of the created particles, we selected two snapshots during the linear growth phase ($t = 8\pi\tau_c$ and $t = 16\pi\tau_c$), as indicated by the markers in Fig. 2. The corresponding momentum and real-space densities are plotted in Fig. 3.

As shown in Figs. 3(a) and 3(c), the electronic momentum density $\rho(p, t)$ features a distinct peak. For $W = 0.3\lambda_c$, the peak remains centered near $0.8c$, whereas for $W = \lambda_c$ it is similar. The stationarity of this peak position over time suggests it is primarily determined by the field parameters

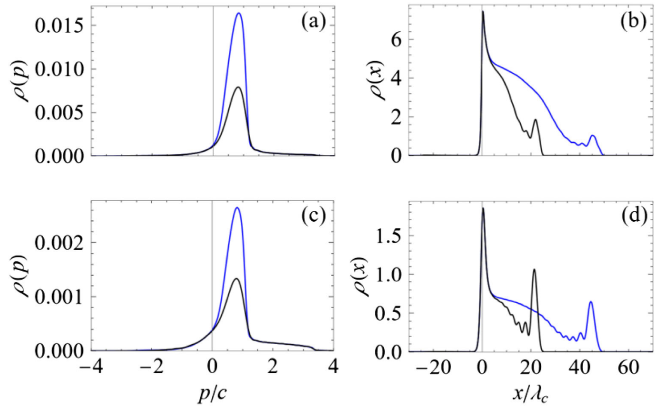


FIG. 3. (a) and (b) show the momentum distribution $\rho(p)$ and spatial distribution $\rho(x)$ for the two points in Fig. 2(a), while (c) and (d) display the corresponding momentum and spatial distributions for the two points in Fig. 2(b).

$E_0$ and $V_0$ rather than the duration of the interaction. The peak magnitude grows linearly in time, consistent with the growth in Fig. 2. Moreover, a broad high-momentum tail ($1.5c - 4c$) is observed. These high-momentum particles are generated during the initial field onset and propagate with constant velocity thereafter.

The real-space distributions $\rho(x, t)$ [Figs. 3(b) and 3(d)] exhibit a primary maximum at the center of the potential ($x = 0$), where the electric field is largest. Following the interpretation in Ref. [38], these correspond to "ghost states"—virtual particles that remain localized at the interface of the positive and negative energy continua.

A second prominent peak in the spatial density propagates away from the interaction zone. These peaks correspond to particles created at the beginning of the interaction, which relate to the high-momentum tail seen in panel (a) and (c). As time progresses, these peaks broaden but the position keep the same for different field width. This is because that these electrons acquire the momentum during the onset of the field, which is independent of the electric field width. Notably, the spatial density decreases as the field width $W$ increases, consistent with the reduction in the total production rate.

While the single-particle distributions $\rho(p, t)$ and $\rho(x, t)$ provide insights into the localization and transport of the created flux, they treat electrons and positrons as independent entities. However, in the Schwinger process, pairs are created at the same space-time region, suggesting that intrinsic quantum correlations are inevitable.

Such correlations represent an additional degree of freedom that remains largely unexplored in the context of supercritical tunneling. In the following sections, we move beyond single-particle observables to derive the mutual correlation functions in both real and momentum space, providing a more complete description of the correlated nature of the vacuum decay.

## III. THE SPACE AND MOMENTUM CORRELATIONS BETWEEN ELECTRONS AND POSITRONS

To quantify the mutual dependence between the created electrons and positrons, we define two-particle correlation functions in both momentum and real space.

The electron-positron correlation operator in momentum space is defined by an antisymmetrized product of the time-dependent creation operators,

$$\hat{O}(p, q; t) = \frac{1}{2}\left[\hat{b}_p^\dagger(t)\hat{d}_q^\dagger(t) - \hat{d}_q^\dagger(t)\hat{b}_p^\dagger(t)\right], \tag{9}$$

where $p$ and $q$ denote the momenta of the electron and positron, respectively. The mutual correlation function, representing the anomalous pair-correlation density in momentum space, is obtained from its vacuum expectation value,

$$\rho(p, q; t) = |\langle \mathrm{vac}|\hat{O}(p, q; t)|\mathrm{vac}\rangle|^2. \tag{10}$$

Utilizing the expansion of the time-dependent operators in terms of the transition matrix $G(\xi, \zeta)$ [Eqs. (4) and (5)], the correlation function can be expressed as,

$$\rho(p, q; t) = \sum_{p_1, p_2} G(q, p_1)G^*(p, p_1)G^*(q, p_2)G(p, p_2). \tag{11}$$

This equation quantifies the statistical relationship between electrons and positrons created with specific momenta. A nonvanishing $\rho(p, q; t)$ indicates that the detection of an electron with momentum $p$ is intrinsically linked to the presence of a positron with momentum $q$.

Analogously, we can define the spatial correlation operator to investigate the relative localization of the created pairs. First, we identify the electronic and positronic components of the field operator $\hat{\Psi}_p^\dagger(x_p, t) = \sum_{p_1} \hat{b}_{p_1}^\dagger(t)\varphi_{p_1}^*(x_p)$ and $\hat{\Psi}_q^\dagger(x_q, t) = \sum_{q_1} \hat{d}_{q_1}^\dagger(t)\varphi_{q_1}^*(x_q)$, respectively. The spatial correlation operator for the electron-positron pair is then defined as,

$$\hat{O}(x_p, x_q; t) = \frac{1}{2}\left[\hat{\Psi}_p^\dagger(x_p, t)\hat{\Psi}_q^\dagger(x_q, t) - \hat{\Psi}_q^\dagger(x_q, t)\hat{\Psi}_p^\dagger(x_p, t)\right], \tag{12}$$

where $x_p$ and $x_q$ denote the position of the electron and positron, respectively. The vacuum expectation value of this operator yields the joint spatial distribution

$$\rho(x_p, x_q; t) = |\langle \mathrm{vac}|\hat{O}(x_p, x_q; t)|\mathrm{vac}\rangle|^2$$
$$= \sum_{q,q'} \left[\sum_{q_1} G(q_1, q)\varphi_{q_1}(x_q)\right]\left[\sum_{p_1} G(p_1, q)\varphi_{p_1}(x_p)\right]^* \left[\sum_{q_2} G(q_2, q')\varphi_{q_2}(x_q)\right]^* \left[\sum_{p_2} G(p_2, q')\varphi_{p_2}(x_p)\right]. \quad (13)$$

These formulations allow for a systematic analysis of the correlation effect in pair production processes. The momentum correlation function $\rho(p, q; t)$ reveals the underlying energy-momentum conservation laws governing the tunneling process. Since electrons and positrons are accelerated in opposite directions by the electric field, their momenta possess opposite signs. Under the condition of a constant potential height $V_0$, the total energy available for the pair is constrained by the effective relation $E_p + E_q \approx V_0$. Using the relativistic energy-momentum relation $E^2 = (pc)^2 + c^4$, we can predict the correlation peaks.

For a potential height $V_0 = 2.5c^2$, the maximum probability occurs when the energy is partitioned equally, $E_p = E_q = V_0/2 = 1.25c^2$. This yields a characteristic momentum $p = \sqrt{(1.25c^2)^2 - c^4}/c = 0.75c$, which is in excellent agreement with the numerical results shown in Fig. 4, where the correlation peak is centered at $p \approx -q \approx 0.75c$. Furthermore, while the peak position is determined by $V_0$, we observe a significant spectral broadening in the positron momentum for a fixed electron momentum. This broadening indicates that the momenta of the individual particles in a pair are not strictly entangled in a delta-function sense but exhibit a quantum mechanical uncertainty inherent to the localized production volume.

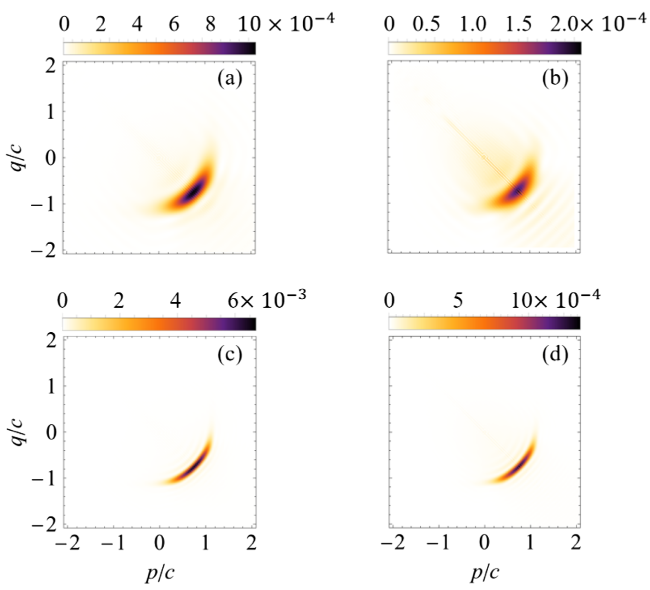


FIG. 4. Correlation function of the created electrons and positrons in momentum space. (a) $W = 0.3\lambda_c$, $t = 8\pi\tau_c$; (b) $W = \lambda_c$, $t = 8\pi\tau_c$; (c) $W = 0.3\lambda_c$, $t = 20\pi\tau_c$; (d) $W = \lambda_c$, $t = 20\pi\tau_c$. The other parameters are the same as in Fig. 2.

The influence of field parameters are also evident. Comparing Figs. 4(a) and 4(b), an increase in $W$ (which corresponds to a decrease in $E_0$) results in a sharp reduction in correlation density, consistent with the exponential suppression predicted by the Schwinger formula. As shown in Figs. 4(a) and 4(c), extending the interaction time leads to a cumulative increase in the joint probability density, with the correlation profile concentrating within the kinematically allowed regions.

The spatial correlation function $\rho(x_p, x_q; t)$ provides a direct visualization of the spatial separation and mutual influence of the particles as they emerge from the supercritical field region. A primary feature of these results is the strong central aggregation at the heart of the electric field ($x \approx 0$), where the coupling between the vacuum and the external field is maximal. This region serves as the "hot zone" for pair production, exhibiting the highest probability of simultaneous electron-positron occurrence.

The spatial correlation is also highly sensitive to the field geometry and interaction duration. Increasing the field width $W$ from $0.3\lambda_c$ to $\lambda_c$ [Figs. 5(a) and 5(b)] significantly reduces the peak correlation probability. This suggests that a wider, less intense field weakens the spatial coupling between the nascent electron and positron.

A key finding of this work is the evolution of the correlation over time. As seen in Figs. 5(a) and 5(c), extending the interaction time does not diminish the maximum correlation amplitude. Instead, it significantly expands the spatial range—the correlation length—over which the pairs remain linked. Even as the particles propagate away from the interaction region into the asymptotic field-free zones, the correlation strength remains robust. This confirms that the pair correlations generated at the moment of creation is preserved during the subsequent dynamical evolution. This persistence is crucial for potential experimental detection, as it implies that correlation signatures can survive long enough to be measured by distant detectors.

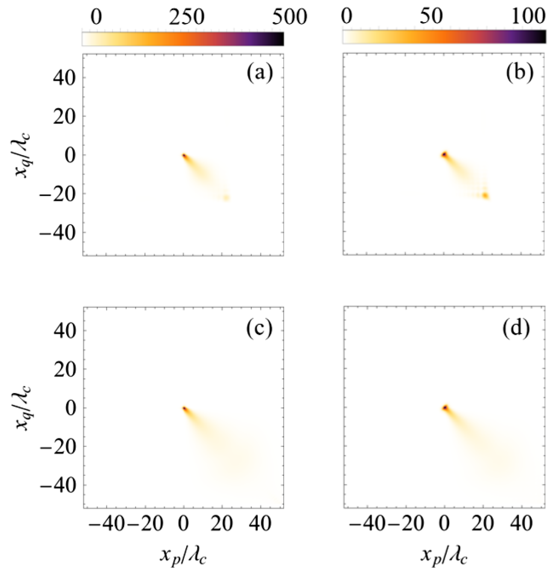


FIG. 5. Correlation function $\rho(x_p, x_q; t)$ of the created electrons and positrons in real space. The parameters are the same as in Fig. 4.

## IV. MARGINAL SPACE AND MOMENTUM CORRELATION FUNCTIONS FOR PARTICLE PAIRS

To further elucidate the nature of the electron-positron correlation, we compute the marginal momentum and spatial distributions. These reduced distributions are obtained by integrating the joint correlation functions over the states of the partner particle, allowing us to compare the correlated pair yield with the total single-particle densities derived in Sec. II.

The marginal momentum distribution for the created electrons is obtained by integrating the joint probability $\rho(p, q; t)$ over all positronic momentum $q$,

$$\rho_{\rm marg}(p; t) = \sum_q \rho(p, q; t) = \sum_q |G(p, q)|^2 - \sum_{p'} \left| \sum_q G(p', q) G^*(p, q) \right|^2. \tag{14}$$

In this equation, the first term represents the standard single-particle occupation probability at momentum $p$. The second term acts as a many-body correlation correction, arising from the intrinsic structure of the vacuum. Following a symmetric derivation, the marginal momentum distribution for positrons is given by summing over the electronic states $p$,

$$\rho_{\rm marg}(q; t) = \sum_p \rho(p, q; t) = \sum_p |G(q, p)|^2 - \sum_{q'} \left| \sum_p G(q', p) G^*(q, p) \right|^2. \tag{15}$$

These reduced distributions quantify the portion of the momentum spectrum that is specifically tied to the production of entangled pairs, excluding the background fluctuations of the vacuum.

The spatial localization of individual particles within the correlated pairs is analyzed by integrating the joint spatial density $\rho(x_p, x_q; t)$. The marginal spatial distributions for electrons and positrons are defined, respectively, as,

$$\rho_{\rm marg}(x_p; t) = \int dx_q \rho(x_p, x_q; t) = \sum_q \left| \sum_{p_1} G(p_1, q) \varphi_{p_1}(x_p) \right|^2 - \sum_{p'} \left| \sum_{p_1, q} G(p', q) G^*(p_1, q) \varphi_{p_1}(x_p) \right|^2, \tag{16}$$

$$\rho_{\rm marg}(x_q; t) = \int dx_p \rho(x_p, x_q; t) = \sum_p \left| \sum_{q_1} G(q_1, p) \varphi_{q_1}(x_q) \right|^2 - \sum_{q'} \left| \sum_{q_1, p} G(q', p) G^*(q_1, p) \varphi_{q_1}(x_q) \right|^2. \tag{17}$$

As compared with the single-particle distribution in Sec. II, the integrated correlation functions $\rho_{\rm marg}$ are strictly smaller than the corresponding single-particle distributions $\rho(x, t)$ and $\rho(p, t)$. This discrepancy is a direct consequence of the vacuum correlation between virtual pairs. In the supercritical regime, the field does not only create real, asymptotic particles but also induces a significant modification of the vacuum. The correction terms in Eqs. (14)–(17) effectively "filter out" the contributions from virtual processes and ghost states that do not result in the simultaneous detection of a correlated pair. Consequently, the reduced distributions provide a cleaner signature of the correlation effects induced by the Schwinger mechanism in quantum vacuum, highlighting the particles that are genuinely born from the same quantum tunneling event. Our results indicate that while the single-particle density is dominated by the localized field center, the correlated portion of the density exhibits the most robust propagation characteristics, facilitating its potential identification in high-intensity laser experiments.

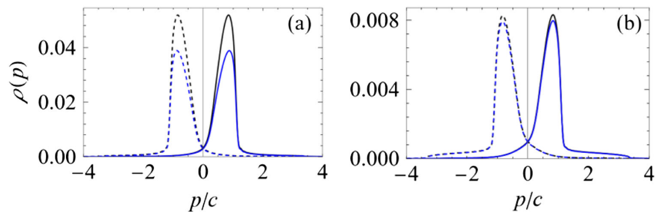


FIG. 6. Comparison of single-particle momentum distributions (black curves) with the marginal correlation functions (blue curves) in momentum space. Solid lines represent electrons and dashed lines represent positrons. (a) $W = 0.3\lambda_c$, $t = 20\pi\tau_c$; (b) $W = \lambda_c$, $t = 20\pi\tau_c$.

A salient feature of the numerical results is the perfect mirror symmetry between the electronic and positronic distributions. This symmetry is an expected consequence of charge conjugation in the Schwinger process, reflecting the interdependent kinematic signatures of the created pairs. The momentum distributions are consistently symmetric relative to the center of the electric field ($p = 0$ in the center-of-mass frame), underscoring the collective nature of the vacuum decay.

The strength of the correlation effect varies significantly across the spectral range, see Fig. 6. In the high-momentum tail ($1.5c - 4.0c$), the correlation between species is relatively weak, and the marginal distribution $\rho_{\mathrm{marg}}(p;t)$ closely follows the total single-particle density $\rho(p,t)$. However, near the distribution peaks ($p \approx 0.75c$), the density accounting for correlations is significantly lower than the uncorrelated single-particle density. This discrepancy highlights the role of the many-body correction term in Eq. (14), which effectively filters out vacuum fluctuations that do not constitute a real particle pair.

The degree of momentum conservation is strictly tied to the spatial extension $W$ of the potential barrier. For narrow barriers, the momentum conservation condition is relaxed due to the high degree of spatial localization (consistent with the uncertainty principle). In this regime, a single negative-energy state can transition into a broad spectrum of positive-energy states. This leads to a significant divergence between the marginal correlation (blue) and single particle distribution (black) curves, as many-body effects are enhanced. As the barrier width increases, the field tends to the uniform case. Consequently, the momentum conservation law becomes increasingly stringent. In this limit, the kinematic constraints force a one-to-one mapping between the electron and positron momenta, causing the correlated and uncorrelated distributions to converge.

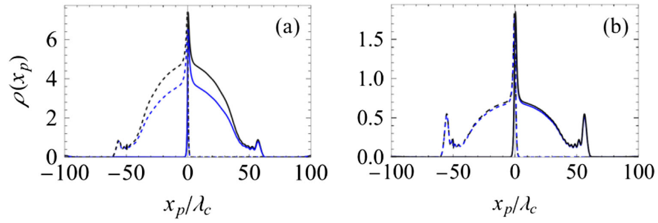


FIG. 7. Comparison of single-particle spatial distributions (black curves) with the marginal correlation functions (blue curves) in real space. Remaining details are the same as in Fig. 6.

The correlation effects in the spatial domain exhibit a distinct dependence on field geometry, as shown in Fig. 7. Within the interaction zone, there is only a slight deviation between the total spatial density and the correlated marginal distribution. This is due to the high degree of wavefunction overlap between electronic and positronic states during the tunneling process, which significantly amplifies quantum correlations. In contrast, outside the potential well, these two distributions diverge sharply. In these field-free regions, the particles behave as quasi-independent entities; meanwhile, the correlations induced by virtual pairs in the vacuum remain, which markedly suppresses the marginal spatial density relative to the total density.

Increasing the field width $W$ tends to reduce spatial localization and weaken wave function overlap. As the production zone broadens, the peak density diminishes, and the spatial "coupling" between the nascent pair is diluted. Consequently, the correlation strength across different spatial regions is reduced as the field becomes more diffuse. Our analysis suggests that the most prominent signatures of quantum correlation emerge in highly localized, supercritical pulses, where the field intensity maximizes many-body corrections.

## V. SUMMARY AND OUTLOOK

In conclusion, we have presented a comprehensive analysis of the quantum correlations between electron-positron pairs generated via the Schwinger mechanism in localized supercritical electric fields. By employing the computational quantum field theory framework, we successfully mapped the evolution of these correlations in both the momentum and spatial domains.

Our investigation has yielded several key insights into the many-body dynamics of vacuum decay. First of all, for a fixed potential height $V_0$, increasing the field width $W$ reduces the effective field strength, leading to an exponential suppression of the quantum correlation, while the total correlation grows linearly with the interaction time. This is consistent with the single particle distribution. Secondly, a central finding is that the momentum and position of a created particle do not dictate definite values for its partner. Instead, the associated particle is characterized by a joint probability distribution. This reflects the intrinsic quantum uncertainty and entanglement born from the nonperturbative tunneling process. In real space, the correlation function exhibits a robust persistence. While the distribution undergoes spatial spreading as the pairs propagate away from the "hot zone," the correlation amplitude remains stable. This indicates that quantum correlations are not merely transient artifacts of the interaction but are preserved as the particles enter the asymptotic, field-free regime. Finally, we found that the correlation effect is most pronounced in highly localized fields. As the electric field width $W$ increases and the field approaches a uniform limit, the marginal distributions converge toward the single-particle densities. This suggests that the spatial gradients of the field are essential for enhancing the many-body corrections to the vacuum response.

These results provide a new theoretical perspective on the structure of the quantum vacuum under extreme conditions. By identifying the specific field parameters that maximize or suppress correlation effects, our work points toward potential experimental strategies for regulating pair production in high-intensity laser-matter interactions. Furthermore, the robustness of these correlations suggests that two-particle coincidence measurements could serve as a high-fidelity diagnostic tool for verifying the nonperturbative Schwinger process in future experimental facilities.

## ACKNOWLEDGMENTS

This work was supported by the National Natural Science Foundation of China (Grants No. 12475251 and No. 12304337), the Natural Science Foundation of Hebei Province (Grant No. A2025502023), and the Fundamental Research Funds for the Central Universities (Grant No. 2025MS180).

## DATA AVAILABILITY

The data that support the findings of this article are not publicly available upon publication because it is not technically feasible and/or the cost of preparing, depositing, and hosting the data would be prohibitive within the terms of this research project. The data are available from the authors upon reasonable request.


[1] C. Radin, Correlations in classical ground states, J. Stat. Phys. **43**, 707 (1986).

[2] S. L. Luo and N. Li, Quantum correlations reduce classical correlations with ancillary systems, Chin. Phys. Lett. **27**, 120304 (2010).

[3] D. Ruelle, Identities for correlation functions in classical statistical mechanics and the problem of crystal states, J. Stat. Phys. **180**, 1002 (2020).

[4] C. Riek, P. Sulzer, M. Seeger, A. S. Moskalenko, G. Burkard, D. V. Seletskiy, and A. Leitenstorfer, Subcycle quantum electrodynamics, Nature (London) **541**, 376 (2017).

[5] A. I. Lvovsky and M. G. Raymer, Continuous-variable optical quantum-state tomography, Rev. Mod. Phys. **81**, 299 (2009).

[6] S. B. Pope, *Turbulent Flows* (Cambridge University Press, 2000)

[7] J. K. Bhattacharjee and D. J. Scalapino, Time-dependent velocity correlation functions of randomly stirred fluids from mode coupling theories, Phys. Lett. **85A**, 442 (1981).

[8] R. Dorner and V. Vedral, Correlations in quantum physics, Int. J. Mod. Phys. B **27**, 1345017 (2013).

[9] A. Okopińska and P. Kościk, Correlation and entanglement in elliptically deformed two-electron quantum dots, Few-Body Syst. **50**, 413 (2011).

[10] P. Bracken, Bell's inequalities and methods of quantifying measures of entanglement correlations, Int. J. Theor. Phys. **53**, 2819 (2014).

[11] K. C. Tan, H. Kwon, C.-Y. Park, and H. Jeong, Unified view of quantum correlations and quantum coherence, Phys. Rev. A **94**, 022329 (2016).

[12] S. Haddadi, M. R. Pourkarimi, A. Akhound, and M. Ghominejad, Quantum correlations and quantum-memory-assisted entropic uncertainty relation in two kinds of spin squeezing models, Laser Phys. Lett. **16**, 095202 (2019).

[13] M. Gessner, E.-M. Laine, H.-P. Breuer, and J. Piilo, Correlations in quantum states and the local creation of quantum discord, Phys. Rev. A **85**, 052122 (2012).

[14] C. Banerjee, M. P. Singh, and A. M. Fedotov, Phase control of Schwinger pair production by colliding laser pulses, Phys. Rev. A **98**, 032121 (2018).

[15] Y. Li, Y. Dai, and Y. Shi, Pairwise mode entanglement in Schwinger production of particle-antiparticle pairs in an electric field, Phys. Rev. D **95**, 036006 (2017).

[16] Y. Li, Q. Mao, and Y. Shi, Schwinger effect of a relativistic boson entangled with a qubit, Phys. Rev. A **99**, 032340 (2019).

[17] S. M. Wu, J. X. Li, X. W. Fan, W. M. Li, X. L. Huang, and H. S. Zeng, Dynamic entanglement for continuous variables in an electric field background, Commun. Theor. Phys. **75**, 065103 (2023).

[18] H. S. Zeng and L. J. Wu, Hybrid relativistic effect of the entangled fermion fields, Eur. Phys. J. Plus **138**, 814 (2023).

[19] T. Fan, Q. Liu, J. Jing, and J. Wang, Quantum metrology of Schwinger effect, Eur. Phys. J. C **84**, 896 (2024).

[20] D. Kranas, A. Marchon, and S. Pla, Entanglement in the Schwinger effect, arXiv:2512.10091.

[21] S. M. Wu and H. S. Zeng, Schwinger effect of Gaussian correlations in constant electric fields, Classical Quantum Gravity **37**, 115003 (2020).

[22] S. Kaushal, Fermionic entanglement in the presence of background electric and magnetic fields, Eur. Phys. J. C **85**, 75 (2025).

[23] M. M. Majczak, K. Krajewska, A. Bechler, and J. Z. Kamiński, Spirals, vortices, and helicity entanglements in dynamical Sauter-Schwinger pair creation, Phys. Rev. A **113**, 052224 (2026).

[24] T. Cheng, Q. Su, and R. Grobe, Introductory review on quantum field theory with space-time resolution, Contemp. Phys. **51**, 315 (2010).

[25] R. E. Wagner, M. R. Ware, E. V. Stefanovich, Q. Su, and R. Grobe, Local and nonlocal spatial densities in quantum field theory, Phys. Rev. A **85**, 022121 (2012).

[26] Q. Z. Lv and H. Bauke, Time- and space-resolved selective multipair creation, Phys. Rev. D **96**, 056017 (2017).

[27] J. W. Braun, Q. Su, and R. Grobe, Numerical approach to solve the time-dependent Dirac equation, Phys. Rev. A **59**, 604 (1999).

[28] A. D. Bandrauk and H. Shen, High-order split-step exponential methods for solving coupled nonlinear Schrodinger equations, J. Phys. A **27**, 7147 (1994).

[29] B. Thaller, *The Dirac Equation*, Theoretical and Mathematical Physics (Springer, Berlin, Heidelberg, 1992).

[30] A. Wachter, *Relativistic Quantum Mechanics*, Theoretical and Mathematical Physics (Springer, Dordrecht, 2010).

[31] F. Sauter, Über das verhalten eines elektrons im homogenen elektrischen feld nach der relativistischen theorie diracs, Z. Phys. **69**, 742 (1931).

[32] H. Gies and K. Klingmüller, Pair production in inhomogeneous fields, Phys. Rev. D **72**, 065001 (2005).

[33] Q. Su, W. Su, Q. Z. Lv, M. Jiang, X. Lu, Z. M. Sheng, and R. Grobe, Magnetic control of the pair creation in spatially localized supercritical fields, Phys. Rev. Lett. **109**, 253202 (2012).

[34] Q. Z. Lv, Q. Su, and R. Grobe, Manipulation of the vacuum to control its field-induced decay, Phys. Rev. Lett. **121**, 183606 (2018).

[35] A. Chervyakov and H. Kleinert, On electron–positron pair production by a spatially inhomogeneous electric field, Phys. Part. Nucl. **49**, 374 (2018).

[36] M. Ababekri, B.-S. Xie, and J. Zhang, Effects of finite spatial extent on Schwinger pair production, Phys. Rev. D **100**, 016003 (2019).

[37] S. P. Kim and C. Schubert, Nonadiabatic quantum Vlasov equation for Schwinger pair production, Phys. Rev. D **84**, 125028 (2011).

[38] P. Krekora, Q. Su, and R. Grobe, Interpretational difficulties in quantum field theory, Phys. Rev. A **73**, 022114 (2006).